Research Square

Preprints are preliminary reports that have not undergone peer review.
They should not be considered conclusive, used to inform clinical practice,
or referenced by the media as validated information.

Scalable two-step annealing method for preparing ultra-high-density single-atom catalyst libraries

Jiong Lu (chmluj@nus.edu.sg)
Department of Chemistry, National University of Singapore https://orcid.org/0000-0002-3690-8235
Xiao Hai
National University of Singapore https://orcid.org/0000-0002-7631-9769
Shibo Xi
Institute of Chemical and Engineering Sciences https://orcid.org/0000-0002-8521-3237
Sharon Mitchell
ETH Zurich
Karim Harrath
Southern University of Science and Technology
Haomin Xu
National University of Singapore https://orcid.org/0000-0003-3704-1810
Dario Akl
ETH Zurich
Debin Kong
National Center for Nanoscience and Technology
Jing Li
National University of Singapore https://orcid.org/0000-0002-5627-4153
Zejun Li
National University of Singapore
Tao Sun
National University of Singapore
Huimin Yang
National University of Singapore https://orcid.org/0000-0003-4949-0787
Yige Cui
National University of Singapore
Chenliang Su
Shenzhen University https://orcid.org/0000-0002-8453-1938
Xiaoxu Zhao
Nanyang Technological University
Jun Li
Tsinghua University https://orcid.org/0000-0002-8456-3980
Javier Pérez-Ramírez

ETH Zurich https://orcid.org/0000-0002-5805-7355

Article

Keywords:

Posted Date: April 14th, 2021

DOI: https://doi.org/10.21203/rs.3.rs-394916/v1

License: This work is licensed under a Creative Commons Attribution 4.0 International License.
Read Full License

Version of Record: A version of this preprint was published at Nature Nanotechnology on November 25th, 2021. See the published version at https://doi.org/10.1038/s41565-021-01022-y.

Abstract

The stabilization of transition metals as isolated centres on suitably tailored carriers with high density is crucial to exploit the technical potential of single-atom heterogeneous catalysts, enabling their maximized productivity in industrial reactors. Wet-chemical methods are best suited for practical applications due to their amenability to scale up. However, achieving single-atom dispersions at metal contents above 2 wt.% remains challenging. We introduce a versatile approach combining impregnation and two-step annealing to synthesize ultra-high-density single-atom catalysts (UHD-SACs) with unprecedented metal contents up to 23 wt.% for 15 metals on chemically-distinct carriers. Translation to an automated protocol demonstrates its robustness and provides a path to explore virtually unlimited libraries of mono or multimetallic catalysts. At the molecular level, characterization of the synthesis mechanism through experiments and simulations shows that controlling the bonding of metal precursors with the carrier via stepwise ligand removal prevents their thermally-induced aggregation into nanoparticles, ensuring atomic dispersion in the resulting UHD-SACs. The catalytic benefits of UHD-SACs are demonstrated for the electrochemical reduction of CO_2 to CO over NiN_4 motifs on carbon.

Main

Improving atom economy of chemical transformations and ensuring the maximal utilization of scarce catalytic materials are central targets for sustainable chemistry[1-5]. Heterogeneous single-atom catalysts (SACs), integrating monodisperse atomic metal centers with tailorable coordination environments, demonstrate promising potential to fulfill both of these objectives in several energy-related transformations[6-14]. A fundamental challenge for implementing this pioneering class of catalysts in many technical applications is the lack of synthetic routes enabling their preparation with high surface densities of metal[15-17]. The latter is particularly important to maximize the productivity per unit reactor volume or area in large-scale processes. Taking nickel SACs, which exhibit highly selective performance in the electrochemical reduction of carbon dioxide[18], as a representative example, a literature analysis shows that most of the materials reported to date are based on carbon-related materials and contain metal contents centered around 1 wt.%, with exceptional cases up to 7 wt.% (**Fig. 1a**). These values are significantly lower than the expected theoretical capacity of these carriers for anchoring metal atoms.

Of the distinct synthesis strategies reported for SACs, the post-synthetic introduction of metals via wet deposition routes such as impregnation is among the most amenable to scale up[19-29]. It also favors surface localization, unlike direct synthesis approaches such as pyrolysis, where a large fraction of the active phase may become embedded in the bulk of carrier materials[30]. However, when introducing high contents, it is difficult to prevent the undesired aggregation of metal species into clusters and nanoparticles following conventional methods (**Fig. 1b, c**, **Supplementary Fig. 1**). The poor stability is widely attributed to the higher surface energies of isolated metal atoms and is exacerbated by thermal treatments applied to remove ligands from metal precursors[16]. Currently, no study has achieved ultra-high-density SACs, defined herein as having metal contents over 10 wt.% for carbon-based catalysts,

following post-synthetic routes, or demonstrated their enhanced productivity in catalytic applications. Another scarcely addressed aspect is the extension to multimetallic systems, which is relevant for the development of technical catalysts since they often incorporate two or more metals, for example as cocatalysts, promotors or stabilizers. Beyond the selection of carriers with abundant surface anchoring sites for metal atoms, the synthesis mechanism remains poorly understood at the molecular level.

Two-step annealing approach

The two-step annealing approach introduced here comprises a versatile and scalable method for the preparation of mono or multimetallic ultra-high-density single-atom catalysts, denoted with the acronym UHD-SACs, of more than 15 transition metals on carriers with distinct chemical nature such as nitrogen-doped carbon (NC), polymeric carbon nitride (PCN), and metal oxides (**Supplementary Fig. 2**). The approach relies on controlling ligand removal from metal precursors and the associated interactions with the carrier (**Fig. 1d**). In this way, weakly bound metal species can be readily removed by washing, thereby reducing the propensity of the deposited metal atoms to aggregation and permitting the stabilization of much higher metal contents compared to conventional impregnation routes. The method uses aqueous solutions of common metal precursors (chlorides, sulphates, or acetates) or mixtures thereof where multimetallic systems are targeted. To regulate ligand removal, the temperature of the first annealing step (T_1) needs to be lower than that of the decomposition temperature of the precursor. For this reason, the use of metal chlorides provides greater control due to the strong intrinsic metal-chlorine bonds, which permits the use of higher temperatures in the first annealing step (**Supplementary Table 1**). The chemisorbed metal precursors are subsequently transformed into UHD-SACs with well-defined atomic structures by a second annealing step at a higher temperature (T_2) to remove the remaining ligands.

Analysis by inductively coupled plasma atomic emission spectroscopy (ICP-AES) shows that the two-step annealing method achieves metal contents larger than 10 wt.%, in several cases exceeding 20 wt.%, on both NC and PCN carriers for all the metals studied (**Fig. 1e**). Lower metal loadings of between 2-10 wt.% result when using CeO_2 as the carrier, reflecting its higher relative molecular weight than carbon-related materials. To further confirm the generality of the approach, we extended the synthesis to other commonly used supports, including titanium dioxide and alumina (**Supplementary Fig. 3**). Additionally, the simultaneous introduction of multiple metal precursors behaves additively and successfully yields multimetallic UHD-SACs, demonstrating the scope of the method to produce a widely tunable materials platform (**Supplementary Fig. 4**).

Confirming the ultra-high-density atomic dispersion

The atomic metal dispersions of the obtained UHD-SACs on NC are directly imaged by annular dark field scanning transmission electron microscopy (ADF-STEM, **Fig. 2a**), revealing densely populated features ascribed to isolated atoms. Low-magnification elemental mapping by energy-dispersive X-ray spectroscopy (EDS) of NC-based UHD-SACs confirms the uniform metal distribution and the absence of larger aggregates (**Supplementary Fig. 5**). The bright dots in the high-magnification ADF-STEM images of

Pt on NC, PCN and CeO_2 exhibit diameters of approximately 0.2 nm, matching the expected size of an isolated Pt atom (**Fig. 2b**, **Supplementary Fig. 6**). PCN-supported UHD SACs display high metal atom density (**Supplementary Fig. 7a**) and heavy elements such as W, Ir and Pt, which are distinguishable on CeO_2, also evidence atomic dispersion (**Supplementary Fig. 7b**). Elemental uniformity is also visible at a larger scale, as seen in low-magnification EDS mappings (**Supplementary Figs. 8** and **9**).

Powder X-ray diffraction (XRD) patterns confirm the absence of crystalline metal compounds in all UHD-SACs samples, evidencing only reflections of the carrier materials (**Supplementary Fig. 10 a-c**). The Fourier transformed extended X-ray absorption fine structure (EXAFS) spectra of all the UHD-SACs samples exhibit major peaks around 1.5 Å, corresponding to M-N/O bond lengths (**Fig. 2c**, **Supplementary Fig. 10 d-f**)[10,31]. No signatures of metal-metal coordination between 2.1 Å and 2.5 Å are observed in any of the samples, confirming the absence of metal nanoparticles or clusters. Consistently, infrared spectroscopy (IR) of adsorbed CO on Pt_1/NC, Pt_1/PCN and Pt_1/CeO_2 reveals only one set of CO absorption bands centred at 2117 cm^{-1} (**Fig. 2d**). No IR peaks in the range of 2070-2090 cm^{-1} corresponding to Pt nanoparticles can be observed[11]. These results further validate the atomic-resolution ADF-STEM analyses, demonstrating the successful preparation of UHD-SACs with various metals and carriers. The Pt L_3-edge X-ray absorption near-edge structure (XANES) spectra and the Pt 4*f* X-ray photoelectron (XPS) spectra both indicate that all the Pt species are positively charged, and the valence state on NC and PCN is slightly lower than on CeO_2 (**Supplementary Fig. 11**)[10,32]. ADF-STEM images and elemental maps of Ni, Pd and Ni, Pd, Pt UHD-SACs also confirmed the atomic dispersion and uniform dispersion of the constituent metals in multimetallic systems (**Fig. 3**)

Amenability to automation and scale-up

Motivated by growing efforts across catalysis research towards automation and standardization of procedures, which are most advanced in computational chemistry and catalyst characterization and testing, we translated the two-step annealing approach to an automated synthesis protocol. The use of a robotic platform (**Fig. 4a**) permits precise control over the quantity and speed of metal addition as well as the extent of sample washing and requires only minor adaptions of the laboratory-based protocol such as the use of shaking instead of sonication for mixing the carrier with the aqueous solution of the metal precursor (**Fig. 4b**). Accordingly, the procedure could readily obtain Ni-SACs over a broad range of metal contents (**Fig. 4c**). Slightly lower values observed in the samples prepared by the automated compared to the laboratory protocol originate from operating under ambient rather than reduced pressure during the mixing step, which decreases surface wetting of the micropores. Given the virtually limitless potential combinations of metals, carriers, and stoichiometry, the possibility to automate the synthesis protocol enabling the reproducible preparation of well-defined UHD-SAC libraries is highly attractive for the derivation of more precise synthesis-property-performance relationships to guide their design in targeted applications. Besides versatility, another important feature of our approach is the scalability. Since the two-step annealing approach employs simple unit operations (impregnation, thermal treatment, washing,

and filtration), it readily translates to the kilogram scale production of UHD-SACs, with no appreciable differences in the properties of the resulting material (**Supplementary Fig. 12**).

Mechanistic insights into the controlled ligand removal

To understand the greater effectiveness of the two-step annealing strategy, we followed the evolution of the metal and anchor site during the synthesis by EXAFS, XANES, XPS and density functional theory (DFT) modelling. Starting from nickel chloride ($NiCl_2$) and NC, we identify adsorbed $NiCl_2$ ($NiCl_2$/NC), partially chlorinated (NiCl/NC) and the fully bound Ni (Ni_1/NC) single atoms as key intermediates or products, respectively (**Supplementary Fig. 13a**). Whereas XRD analysis of the materials before and after the respective annealing steps confirms the disappearance of characteristic $NiCl_2$ reflections, it provides no information on changes in the local environment (**Supplementary Fig. 13b**). Comparison of both XANES and EXAFS spectra evidences appreciable differences between the intermediates. A single peak at around 1.97 Å for $NiCl_2$/NC corresponds to the Ni-Cl bond from pure $NiCl_2$. After low-temperature annealing, a strong signal appears around 1.40 Å for NiCl/NC, consistent with the newly formed Ni-N bonds[18,33] (**Fig. 5a**). Concurrently, the peak position of Ni-Cl bond moved from 1.97 Å to 1.75 Å, resulting from the transformation of $NiCl_2$/NC to a NiN_4Cl structure. From the fitting results **(Supplementary Fig. 14, Supplementary Table 2**), the coordination numbers of N and Cl atoms in the first coordination sphere of Ni are around 4.8 and 0.9, respectively, with a square-pyramidal configuration for Ni-N bonding. Following the high-temperature annealing forming Ni_1/NC, only the Ni-N peak around 1.40 Å is seen with no evidence of Ni-Cl bonds, indicating that the anchored Ni atoms lose another ligand to form the Ni-N4 site. The profile of the XANES spectrum of Ni_1/NC (**Supplementary Fig. 13c**) contains similar characteristic features to the nickel phthalocyanine (NiPc), which has a well-defined NiN_4 structure[33]. The shoulder at 8340 eV of Ni_1/NC and NiPc is due to a $1s$-$4p_z$ orbital transition characteristic for a square-planar configuration with high D_{4h} local symmetry. This feature is significantly weakened in the NiCl/NC sample, indicating a broken D_{4h} symmetry, which agrees well with our proposed atomic model (NiN_4Cl) in which the Ni-Cl bond displaces the Ni from the N_4 in plane geometry.

Additionally, the structural evolution of the surface anchoring site was investigated by XPS. The high-resolution N $1s$ spectra of the anchor site can be fitted by components corresponding to C=N-C (397.9 eV, marked as N1), C=N-H (399.3 eV, marked as N2), C=N-Ni-Cl (398.3 eV, marked as N3), and C=N-Ni (398.7 eV, marked as N4) species (**Fig. 5b**)[18,34]. In the pristine NC, the anchoring sites are composed of two C=N-C (N1) and two C=N-H (N2). The intensity of N_2 noticeably decreases and is accompanied by a transformation of N1 to N3 during the first-step low-temperature annealing. Concurrently, N-H bonds are suggested to be replaced by newly formed N-Ni bonds (N3). The Ni precursor is expected to react with C=N-H functional groups by breaking the N-H bond and removing the H atom at elevated temperature. In the following high-temperature annealing, the N-H bond completely disappears with the accompanying transformation of N3 to N4, suggesting further cleavage of the remaining N-H groups to form exclusively Ni-N4 sites. The binding energies of Ni $2p_{3/2}$ in NiCl/NC and Ni_1/NC were 855.3 and 855.4 eV, respectively

(**Supplementary Fig. 13d**), which are 1.3 and 1.2 eV lower in the $NiCl_2$ precursor (Ni^{2+}, 856.6 eV). The binding energy of Cl 2$p_{3/2}$ in NiCl/NC (197.4 eV) is 1.6 eV lower than the precursor (199.0 eV, **Supplementary Fig. 13e**). Interestingly, the stepwise removal of chloride ligands can be followed through the Cl 2*p* signal of $NiCl_2$/NC, NiCl/NC and Ni_1/NC, the latter of which shows no peak. These comprehensive structural analyses unambiguously reveal the path of the coordination of nickel atoms from the adsorbed metal precursor, through our proposed intermediate NiN_4Cl and final NiN_4 structures.

Based on these well-established atomic structures, DFT calculations were conducted to gain molecular-level insight into the synthesis mechanism (**Fig. 5c**). In the first step, the anchoring of a single $NiCl_2$ entity to the N4 anchor site in the carrier leads to the first transition state (TS 1) with a barrier of 1.39 eV and endothermic reaction energy of 0.14 eV. The following rearrangement releasing one HCl molecule is exothermic and occurs spontaneously, forming the first intermediate (Int 1). The release of a second HCl molecule drives the transformation of NiCl/NC to Ni/NC (Int2→ Ni/NC) endergonically (-1.74 eV) without an energy barrier. Since the H and Cl atoms need to be on the same side, the rotation of a hydrogen atom from the bottom to the top surface must be considered (Int1 → Int2). This process requires a barrier of 0.72 eV with endothermic reaction energy of 0.28 eV. Hence, the formation of Ni_1/NC proceeds two endothermic and one spontaneous step, which is in line with our experimental procedure, where two annealing steps are needed.

Enhanced productivity of UHD-SACs

As a proof of concept, we chose to evaluate the catalytic performance of the UHD-SACs in the electrochemical CO_2 reduction to carbon monoxide, an application where nickel single atoms demonstrate promising technical potential[35,36]. For the Ni_1/NC catalyst, the only products detected are gas-phase CO and H_2 and no liquids in the voltage range from 0 to -1.15 V versus RHE. The linear sweep voltammetry (LSV) curves reveal significantly higher current density over the UHD Ni_1/NC than the low-density Ni_1/NC (**Fig. 6a**). In terms of Faradaic efficiency (FE) towards CO, the UHD and low density Ni_1/NC catalysts exhibit a maximum of 97 % at around -0.95 and -0.75 V versus RHE, respectively (**Fig. 6b, Supplementary Fig. 15**). Although the Ni content in UHD Ni_1/NC catalyst is 10 times higher than in the low-density Ni_1/NC catalyst, it conserves the high selectivity towards CO. Notably, the UHD Ni_1/NC catalyst still maintains greater than 86% FE even at a very negative potential of -1.15 V versus RHE. DFT modelling reveals the favourable energetics of the CO_2 reduction reaction over parasitic hydrogen formation at the Ni_1/NC site (**Supplementary Fig. 16**). The main advantage of the UHD Ni_1/NC catalyst for CO_2 reduction is that it delivers a much higher CO partial current density (**Fig. 6c**) due to the high abundance of Ni active sites compared to the conventional low-density counterpart. Furthermore, it preserves stable CO_2 reduction at constant current density for CO (20 mA cm^{-2}) during 48 h of continuous operation (**Fig. 6d**). ADF-STEM images measured after the electrochemical stability test show identical well-dispersed Ni atoms as seen in the fresh Ni_1/NC catalyst. The enhanced performance evidenced by these results demonstrates the exciting scope of UHD-SACs to enhance productivity in a broad variety of

catalytic applications in the near future where mono- or multimetallic single atom systems exhibit promising potential.

Discussion

In summary, the scalable wet-chemistry method to prepare UHD-SACs established here across a broad range of transition metals on chemically distinct carriers comprises a breakthrough towards their practical implementation. Our experimental and theoretical analysis showed that the success of the two-step annealing approach at stabilizing high surface densities of isolated metal atoms derives from the selective bonding of metal precursors to the carrier. This controlled interaction enables the removal of weakly interacting species that would otherwise aggregate upon complete decomposition. Besides monometallic systems, a library of multimetallic systems can be readily accessed, evidencing the general applicability of the two-step annealing method. The reproducibility of the synthesis upon automation and at a large scale demonstrates the robustness of the approach, paving the way for the widespread application of UHD-SACs in sustainable chemical and energy transformations.

Methods

Synthesis of nitrogen-doped carbon (NC): A two-dimensional zeolitic imidazolate framework (2D-ZIF-8) was synthesized as the NC precursor. Typically, $Zn(NO_3)_2{\cdot}6H_2O$ (12.75 g) and 2-methylimidazole (29.15 g) were dissolved separately in deionized water (1000 ml). Then the two aqueous solution were rapidly mixed and vigorously stirred for 2 h. The resulting white precipitate was aged undisturbed for 12 h. The product was collected by centrifugation, then washed with water and ethanol, and subsequently dried at 80 °C overnight. To prepare NC, the 2D-ZIF-8 (5 g) was mixed with KCl (100 g) in deionized water (400 ml) and then dried under rotary evaporation. After drying (120 °C overnight), the KCl intercalated powder was heated to 700 °C (heating rate of 2 °C min^{-1}) for 5 h in N_2 flow. The product was washed with hydrochloric acid (2 M), deionized water, and ethanol, then dried at 80 °C overnight.

Synthesis of Ni_1/NC: (30 wt.% metal feeding) $NiCl_2{\cdot}6H_2O$ (174 mg) and NC (100 mg) were dispersed in 20 ml ethanol solution, sonicated for 10 min, and dried by rotary evaporation followed by in an oven at 80 °C. For low-temperature annealing, the powders were heated to 300 °C (5 °C min^{-1} heating rate) for 5 h in N_2 flow. After thorough washing using a water-ethanol mixture, and the dried powders (80 °C) were subjected to a high-temperature annealing at 550 °C (2 °C min^{-1} heating rate) for 5 h in N_2 flow.

Synthesis of polymeric carbon nitride (PCN): Bulk PCN was prepared by calcining dicyandiamide at 550 °C (2.3 °C min^{-1} heating rate) in a crucible for 3 h in static air. Exfoliated PCN was obtained via the thermal exfoliation of PCN at 500 °C (5 °C min^{-1} heating rate) for 5 h in static air.

Synthesis of Ni_1/PCN: (30 wt.% metal feeding) $NiCl_2{\times}6H_2O$ (174 mg and 100 mg PCN are dispersed in 20 ml ethanol solution and sonicated for 10 min, following rotary evaporation to dry. The powders are dried

in an oven at 80 °C. Then, the powders are heated to 450 °C with a heating rate of 5 °C min^{-1} and was kept for 5 h with the protection of N_2 flow. The obtained powders are washed thoroughly using the mixture of water and ethanol and then dried in an oven at 80 °C. Last, the powders are heated to 550 °C with a heating rate of 2 °C min^{-1} and was kept for 5 h with the protection of N_2 flow.

Synthesis of CeO_2: $Ce(CH_3COO)_3 \cdot xH_2O$ was heated in air at 350 °C (5 °C min^{-1} heating rate) for 2 h, then the temperature was increased to 600 °C (5 °C min^{-1} heating rate) for 5 h.

Synthesis of Ni_1/CeO_2: (10 wt.% metal feeding) 45.5 mg $NiCl_2 \cdot 6H_2O$ and 100 mg CeO_2 are dispersed in 20 ml ethanol solution and sonicated for 10 min, followed by rotary evaporation to remove the solvent. The powders are dried in an oven at 80 °C. Then, the powders are heated to 300 °C with a heating rate of 5 °C min^{-1} under static air. The obtained powders are washed thoroughly using the mixture of water and ethanol and then dried in an oven at 80 °C. Last, the powders are heated to 550 °C with a heating rate of 1 °C min^{-1} and was kept for 5 h under static air.

The synthesis of other metal single-atom catalysts follows the same steps by using the appropriate metal precursor, solvent, annealing temperatures and atmospheres.

Automated synthesis

The automated catalyst preparation was carried out in a Chemspeed Flex Isynth synthesis platform. The distinct carriers (100 mg) were dispensed into the reaction block using an in-built extruder for precision dosing. After addition of ethanol (5 ml, ACS reagent grade, Millipore Sigma), the nickel precursor solution ($NiCl_2 \cdot 6H_2O$, 99.9% purity, Sigma Aldrich, in ethanol) of the desired molarity is added gravimetrically (5 ml). The resulting slurries were shaken (300 RPM) for 30 min, and the solvent was subsequently removed under vacuum (80 °C, 7 h). The dry powders were transferred to ceramic boats and annealed in flowing nitrogen (20 ml min^{-1}) at 300 °C (ramp 5 °C min^{-1}). The annealed powders were subsequently washed (water:ethanol, 1:1, 15 ml) and vacuum-filtered (frit pore diameter, 16-40 μm) three times and then dried (80 °C, vacuum) in the synthesis robot. Finally, the powders were subjected to a second annealing step to 550 °C (ramp 2 °C min^{-1}) in flowing N_2 atmosphere.

Material Characterization

Wide-angle X-ray diffraction (XRD) patterns were collected on a Bruker D8 Focus Powder X-ray diffractometer using Cu Kα radiation (40 kV, 40 mA) at room temperature. Transmission electron microscopy (TEM) images were obtained with an FEI Titan 80-300 S/TEM or a Talos F200X instrument both operated at 200 kV. ADF-STEM imaging was carried out in an aberration-corrected JEOL ARM-200F system equipped with a cold field emission gun operating at 60 kV. The images were collected with a half-angle range from ~81 to 280 mrad, and the convergence semiangle was set at ~30 mrad. X-ray photoelectron spectroscopy (XPS) measurements were carried out in a custom-designed ultrahigh-vacuum system with a base pressure lower than 2×10^{-10} mbar. Al Kα ($h\nu$ = 1486.7 eV) was used as the

excitation source for XPS. The metal loadings in all the samples were measured by an inductively coupled plasma atomic emission spectrometer (ICP-AES). N_2 isotherms were measured at -196 °C using a Quantachrome Instruments AutosorbiQ (Boynton Beach, FL). FTIR spectra for CO adsorption were performed at 25 °C on a Bruker Equinox 55 spectrometer equipped with a mercury cadmium telluride detector. The X-ray absorption near-edge structure (XANES) and the extended X-ray absorption fine structure (EXAFS) measurements were carried out at the XAFCA beamline of the Singapore Synchrotron Light Source (SSLS)[37] and Shanghai Synchrotron Radiation Facility (SSRF), Shanghai Institute of Applied Physics (SINAP). Si (111) double crystal monochromator was used to filter the X-ray beam. Metal foils were used for the energy calibration, and all samples were measured under transmission mode at room temperature. EXAFS oscillations χ(k) were extracted and analyzed using the Demeter software package[38].

Quantum-theoretical calculations

All calculations were performed using DFT within spin-polarized Kohn-Sham formalism implemented in the Vienna ab initio simulation package (VASP)[39]. The projector augmented-wave method (PAW)[40,41] was used to represent the core electron states. The generalized gradient approximation (GGA) with Perdew-Burke-Ernzerhof (PBE) exchange-correlation functional[42] and a plane wave representation for the wave function with a cut-off energy of 500 eV were used. Lattice parameters and all atoms were fully relaxed for total energy optimization. The convergence criterion for the maximum residual force and energy was set to 0.02 eV $Å^{-1}$ and 10^{-5} eV, respectively, during the structure relaxation. A 6 × 6 × 1 supercell was used to model the graphene surface and the Brillouin zones were sampled by a Monkhorst-Pack k-point mesh with a 3 × 3 × 1 k-point grid. A 15 Å vacuum space was set, in the *z*-direction, to prevent periodic image interactions. Searches to identify transition states were performed using Climbing Image Nudged Elastic-Band (CI-NEB) and Dimer methods[43,44] and further confirmed by only one imaginary vibrational frequency.

Electrochemical Tests

All CO_2 reduction experiments were performed using a three-electrode system connected to an electrochemical workstation (CHI 760E). Ag/AgCl with saturated KCl solution and platinum mesh served as the reference and counter electrodes, respectively. The electrocatalyst was prepared by mixing the catalyst powder (2 mg), ethanol (1 ml), and Nafion solution (10 µl, 5 wt. %) followed by sonication for 1 h. Then, the catalyst suspension (100 µl) was dropped onto a dry carbon fibre paper (AvCarb P75T, 0.5 cm^2), giving a loading density of 0.4 mg cm^{-2}. All potentials were calculated with respect to the reversible hydrogen electrode (RHE) scale according to the Nernst equation ($E_{RHE} = E_{Ag/AgCl} + 0.0591 \times pH + 0.197$ V, at 25 °C). The electrolyte was 0.5 M $KHCO_3$ saturated with CO_2 having a pH of 7.2. The products and Faradic efficiency of CO_2 reduction were measured using chronoamperometry at each fixed potential in an H-type electrochemical cell separated by a Nafion 117 membrane. Prior to the measurement, the electrolyte was saturated with CO_2 by flowing gas with a rate of 20 ml min^{-1} through the cell for 30 min.

Declarations

Acknowledgments

J.Lu. acknowledges the support from MOE grant (R-143-000-B47-114) and National University of Singapore Flagship Green Energy Program (R-143-000-A55-646). X.Z. thanks the support from the Presidential Postdoctoral Fellowship, Nanyang Technological University, Singapore via grant 03INS000973C150. S.M., D.F.A, and J.P.-R. acknowledge funding from the NCCR Catalysis, a National Centre of Competence in Research funded by the Swiss National Science Foundation. Jun.L acknowledges the financial support by the National Natural Science Foundation of China (Grant 22033005) and the Guangdong Provincial Key Laboratory of Catalysis (No. 2020B121201002). Computational resources were supported by the Center for Computational Science and Engineering (SUSTech) and Tsinghua National Laboratory for Information Science and Technology. We would like to acknowledge the Facility for Analysis, Characterization, Testing and Simulation, Nanyang Technological University, Singapore, for use of their electron microscopy facilities.

Author contributions

X.H. and J.Lu. conceived and designed the experiments. J.P.-R. conceived the automated synthesis protocol. J.Lu. and J.P.-R. supervised the project and organized the collaboration. X.H. performed materials synthesis. S.M. and D.F.A performed automated synthesis. X.H. and T. S. performed the activity test. S.X. performed the XAFS measurement. X.Z., H.X. and D.K. performed the electron microscopy experiments and data analysis. C.S. helped to perform the CO-DRIFTS measurements. Jing.L. performed the XPS measurements. Z.L. performed the N_2 sorption measurements. H.Y. and Y.C. performed the XRD measurements. K.H. and Jun.L. carried out theoretical calculations. X.H., S.M., J.P.-R. and J.Lu. wrote the manuscript. All authors discussed and commented on the manuscript.

Competing interests

The authors declare no competing interest.

References

1 Kaiser, S. K., Chen, Z., Faust Akl, D., Mitchell, S. & Pérez-Ramírez, J. Single-atom catalysts across the periodic table. *Chem. Rev.* **120**, 11703-11809 (2020).

2 Li, Z. *et al.* Well-defined materials for heterogeneous catalysis: from nanoparticles to isolated single-atom sites. *Chem. Rev.* **120**, 623-682 (2019).

3 Li, X., Yang, X., Huang, Y., Zhang, T. & Liu, B. Supported noble-metal single atoms for heterogeneous catalysis. *Adv. Mater.* **31**, 1902031 (2019).

4 Wang, Y. *et al.* Catalysis with two-dimensional materials confining single atoms: concept, design, and applications. *Chem. Rev.* **119**, 1806-1854 (2018).

5 Lin, L. *et al.* Low-temperature hydrogen production from water and methanol using Pt/α-MoC catalysts. *Nature* **544**, 80-83 (2017).

6 Yang, X.-F. *et al.* Single-atom catalysts: a new frontier in heterogeneous catalysis. *Acc. Chem. Res.* **46**, 1740-1748 (2013).

7 Qiao, B. *et al.* Single-atom catalysis of CO oxidation using Pt_1/FeO_x. *Nat. Chem.* **3**, 634-641 (2011).

8 Zhang, L., Zhou, M., Wang, A. & Zhang, T. Selective hydrogenation over supported metal catalysts: from nanoparticles to single atoms. *Chem. Rev.* **120**, 683-733 (2019).

9 Liu, D. *et al.* Atomically dispersed platinum supported on curved carbon supports for efficient electrocatalytic hydrogen evolution. *Nat. Energy* **4**, 512-518 (2019).

10 Jones, J. *et al.* Thermally stable single-atom platinum-on-ceria catalysts via atom trapping. *Science* **353**, 150-154 (2016).

11 Nie, L. *et al.* Activation of surface lattice oxygen in single-atom Pt/CeO_2 for low-temperature CO oxidation. *Science* **358**, 1419-1423 (2017).

12 Wang, A., Li, J. & Zhang, T. Heterogeneous single-atom catalysis. *Nat. Rev. Chem.* **2**, 65-81 (2018).

13 Chen, Z. *et al.* A heterogeneous single-atom palladium catalyst surpassing homogeneous systems for Suzuki coupling. *Nat. Nanotechnol.* **13**, 702-707 (2018).

14 Jung, E. *et al.* Atomic-level tuning of Co-N-C catalyst for high-performance electrochemical H_2O_2 production. *Nat. Mater.* **19**, 436-442 (2020).

15 Beniya, A. & Higashi, S. Towards dense single-atom catalysts for future automotive applications. *Nat. Catal.* **2**, 590-602 (2019).

16 Ji, S. *et al.* Chemical synthesis of single atomic site catalysts. *Chem. Rev.* **120**, 11900-11955 (2020).

17 Ding, S., Hülsey, M. J., Pérez-Ramírez, J. & Yan, N. Transforming energy with single-atom catalysts. *Joule* **3**, 2897-2929 (2019).

18 Yang, H. B. *et al.* Atomically dispersed Ni (I) as the active site for electrochemical CO_2 reduction. *Nat. Energy* **3**, 140-147 (2018).

19 Liu, Y. *et al.* A general strategy for fabricating isolated single metal atomic site catalysts in Y zeolite. *J. Am. Chem. Soc.* **141**, 9305-9311 (2019).

20 Fei, H. *et al.* General synthesis and definitive structural identification of MN_4C_4 single-atom catalysts with tunable electrocatalytic activities. *Nat. Catal.* **1**, 63-72 (2018).

21 He, X. *et al.* A versatile route to fabricate single atom catalysts with high chemoselectivity and regioselectivity in hydrogenation. *Nat. Commun.* **10**, 3663 (2019).

22 Wei, H. *et al.* Iced photochemical reduction to synthesize atomically dispersed metals by suppressing nanocrystal growth. *Nat. Commun.* **8**, 1490 (2017).

23 Yang, H. *et al.* A universal ligand mediated method for large scale synthesis of transition metal single atom catalysts. *Nat. Commun.* **10**, 4585 (2019).

24 Zhang, Z. *et al.* Electrochemical deposition as a universal route for fabricating single-atom catalysts. *Nat. Commun.* **11**, 1215 (2020).

25 Zhao, L. *et al.* Cascade anchoring strategy for general mass production of high-loading single-atomic metal-nitrogen catalysts. *Nat. Commun.* **10**, 1278 (2019).

26 Wei, S. *et al.* Direct observation of noble metal nanoparticles transforming to thermally stable single atoms. *Nat. Nanotechnol.* **13**, 856-861 (2018).

27 Yao, Y. *et al.* High temperature shockwave stabilized single atoms. *Nat. Nanotechnol.* **14**, 851-857 (2019).

28 Liu, P. *et al.* Photochemical route for synthesizing atomically dispersed palladium catalysts. *Science* **352**, 797-800 (2016).

29 Wang, L. *et al.* A sulfur-tethering synthesis strategy toward high-loading atomically dispersed noble metal catalysts. *Sci. Adv.* **5**, eaax6322 (2019).

30 Cheng, Y. *et al.* Atomically dispersed transition metals on carbon nanotubes with ultrahigh loading for selective electrochemical carbon dioxide reduction. *Adv. Mater.* **30**, 1706287 (2018).

31 Zhang, L. *et al.* Direct observation of dynamic bond evolution in single-atom Pt/C_3N_4 catalysts. *Angew. Chem. Int. Ed.* **59**, 6224-6229 (2020).

32 Li, H. *et al.* Synergetic interaction between neighbouring platinum monomers in CO_2 hydrogenation. *Nat. Nanotechnol.* **13**, 411-417 (2018).

33 Avakyan, L. *et al.* Atomic structure of nickel phthalocyanine probed by X-ray absorption spectroscopy and density functional simulations. *Opt. Spectrosc.* **114**, 347-352 (2013).

34 Kabir, S., Artyushkova, K., Serov, A., Kiefer, B. & Atanassov, P. Binding energy shifts for nitrogen-containing graphene-based electrocatalysts-experiments and DFT calculations. *Surf. Interface Anal.* **48**,

293-300 (2016).

35 Jiang, K. *et al.* Isolated Ni single atoms in graphene nanosheets for high-performance CO_2 reduction. *Energy Environ. Sci.* **11**, 893-903 (2018).

36 Kim, H. *et al.* Identification of Single-atom Ni site active toward electrochemical CO_2 conversion to CO. *J. Am. Chem. Soc.* **143**, 925-933 (2021).

37 Du, Y. *et al.* XAFCA: a new XAFS beamline for catalysis research. *J. Synchrotron Radiat.* **22**, 839-843 (2015).

38 Ravel, B. & Newville, M. ATHENA, ARTEMIS, HEPHAESTUS: data analysis for X-ray absorption spectroscopy using IFEFFIT. *J. Synchrotron Radiat.* **12**, 537-541 (2005).

39 Kresse, G. & Furthmüller, J. Efficient iterative schemes for ab initio total-energy calculations using a plane-wave basis set. *Phys. Rev. B* **54**, 11169 (1996).

40 Blöchl, P. E. Projector augmented-wave method. *Phys. Rev. B* **50**, 17953 (1994).

41 Kresse, G. & Joubert, D. From ultrasoft pseudopotentials to the projector augmented-wave method. *Phys. Rev. B* **59**, 1758 (1999).

42 Perdew, J. P., Burke, K. & Ernzerhof, M. Generalized gradient approximation made simple. *Phys. Rev. Lett.* **77**, 3865 (1996).

43 Henkelman, G. & Jónsson, H. A dimer method for finding saddle points on high dimensional potential surfaces using only first derivatives. *J. Chem. Phys.* **111**, 7010-7022 (1999).

44 Henkelman, G., Uberuaga, B. P. & Jónsson, H. A climbing image nudged elastic band method for finding saddle points and minimum energy paths. *J. Chem. Phys.* **113**, 9901-9904 (2000).

Figures

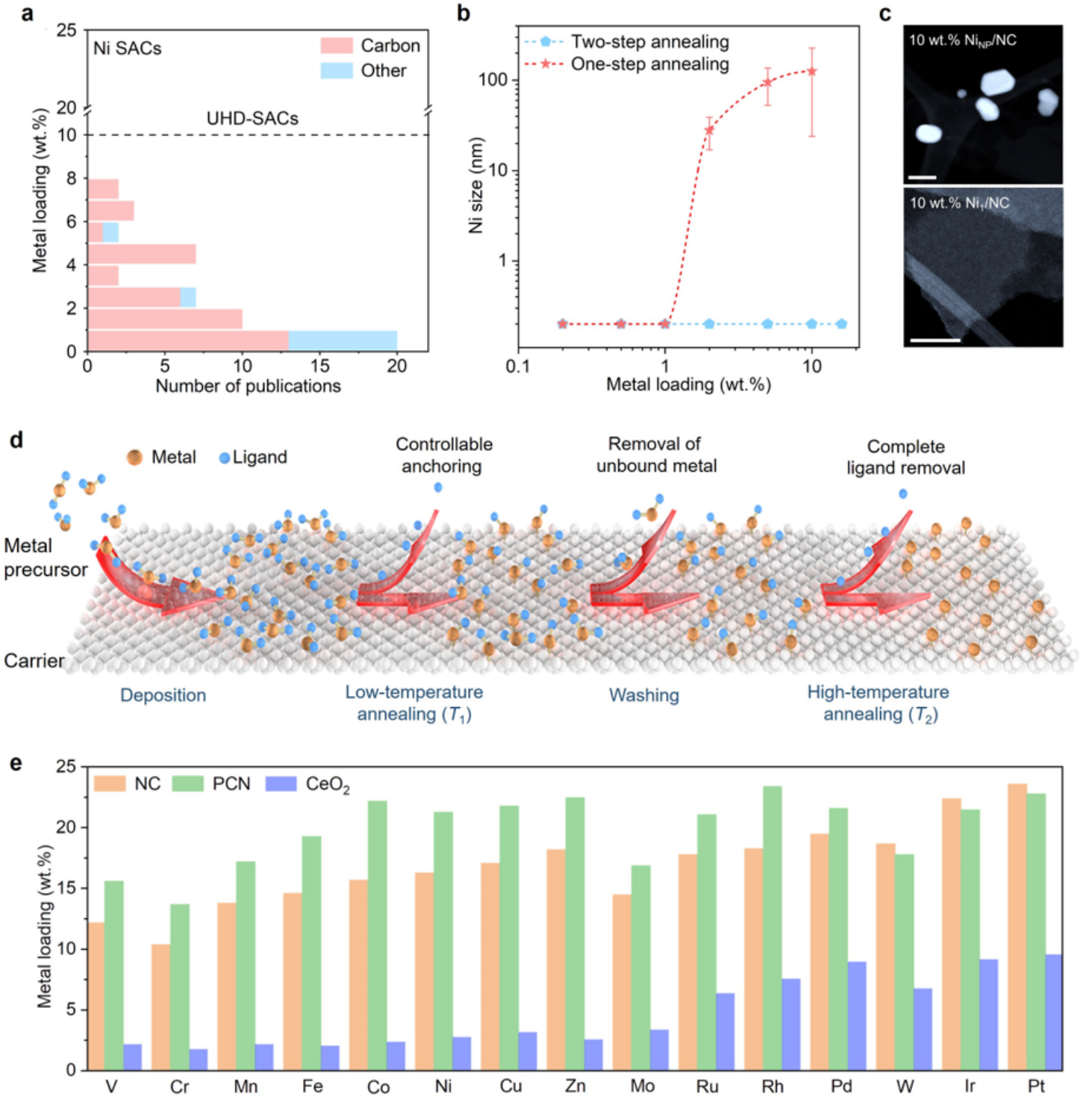

Figure 1

Synthesis of UHD-SACs. a, Literature survey on the metal contents reported in Ni single-atom catalysts revealing the predominant use of carbon-based carriers. b, Comparison of the size of nickel species obtained on NC via a conventional impregnation strategy involving a single thermal treatment and the two-step annealing strategy introduced in this work as a function of the metal content. c, Dark-field TEM images of 10 wt.% Ni-NC samples by a single thermal treatment (top) and two-step (down) annealing

strategy, respectively. d, Strategy for the preparation of UHD-SACs. e, Metal loadings achieved in this study on NC, PCN, and CeO2 supports, respectively.

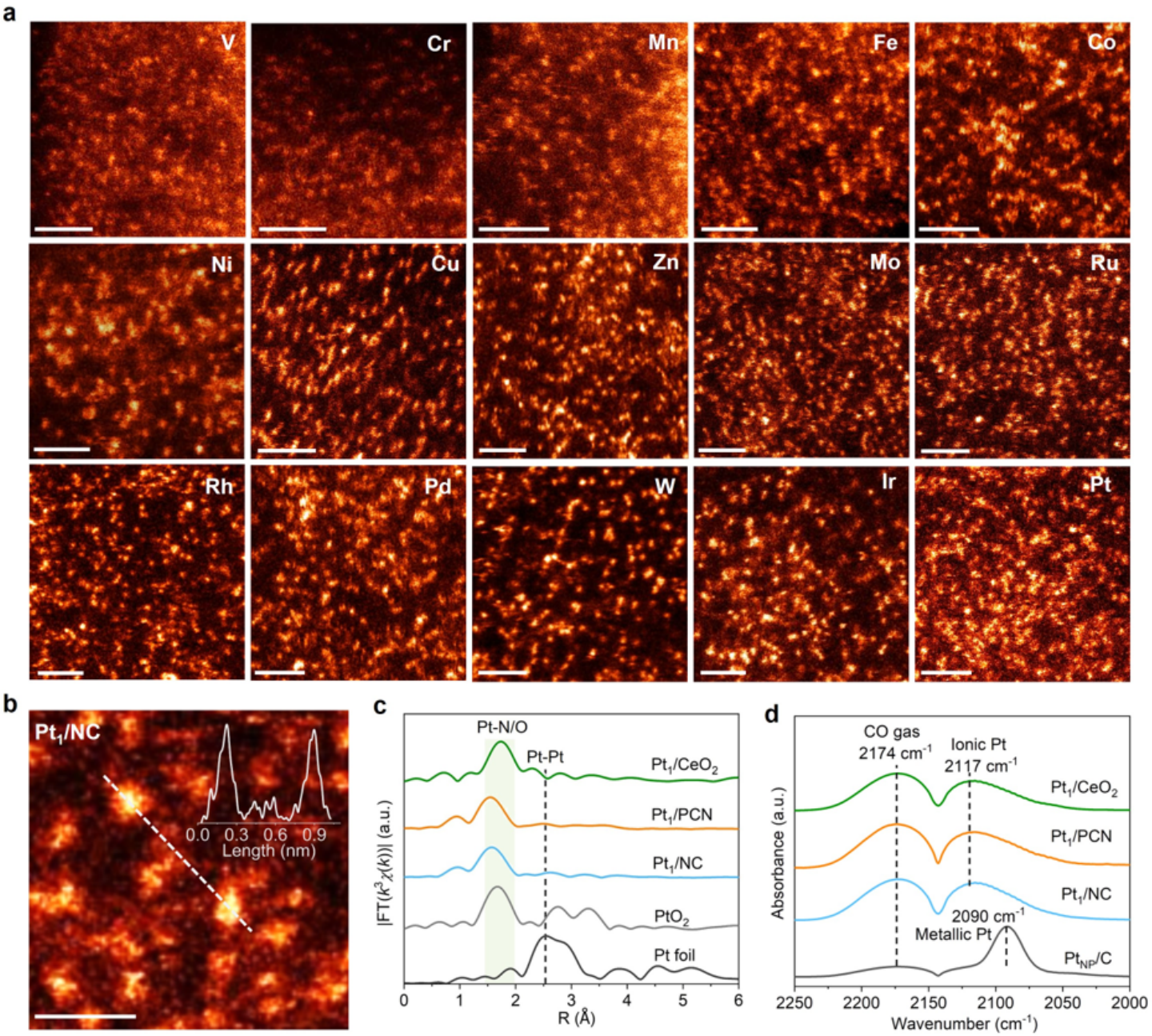

Figure 2

Visualization and spectroscopic characterization of UHD-SACs. a, Atomic-resolution ADF-STEM images of various metals on NC support. Scale bars: 1 nm. b, Enlarged area of the ADF-STEM image of Pt1/NC. Scale bar: 0.5 nm. The inset shows the intensity profile along the dashed white line. c,d, Pt L3-edge Fourier transformed EXAFS spectra (c) and DRIFTS spectra of adsorbed CO (d) of Pt1/NC, Pt1/PCN and Pt1/CeO2 and reference materials.

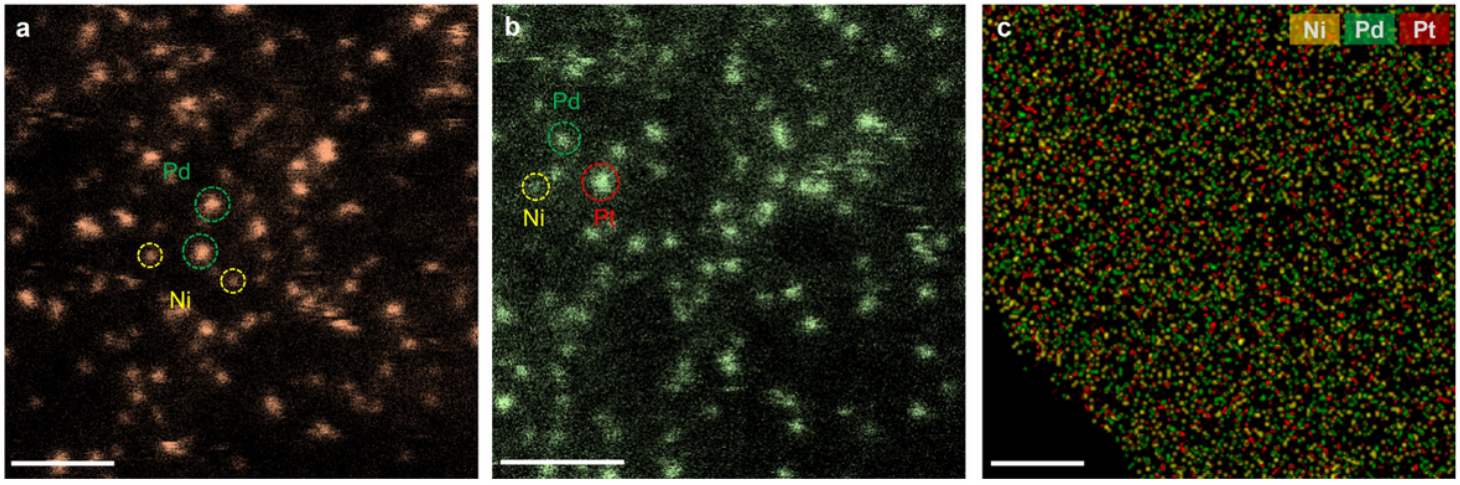

Figure 3

Visualization of multimetallic UHD-SACs. Atomic-resolution ADF-STEM images of a, Ni, Pd and b, Ni, Pd, Pt multimetallic UHD-SACs on NC. c, EDS map of Ni, Pd and Pt in Ni1Pd1Pt1/NC. Scale bars: a-b, 1 nm; c, 100 nm.

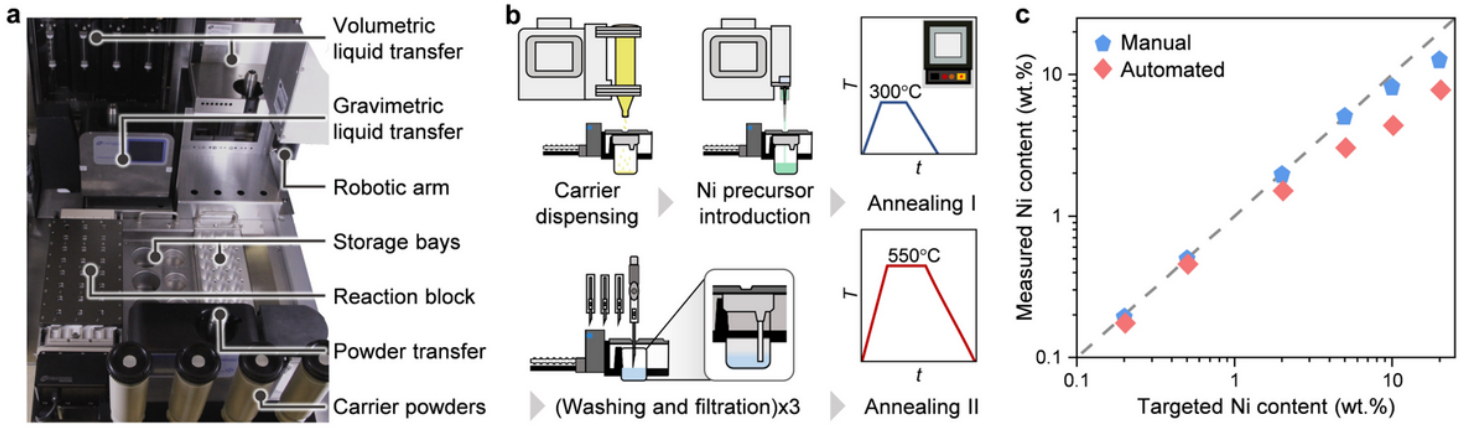

Figure 4

Automated synthesis protocol. a, Photograph of the robotic synthesis platform and assignment of tools to unit operations. b, Flowsheet of the synthesis protocol. c, Comparison of metal contents achieved by automated and manual synthesis of Ni1/NC catalysts.

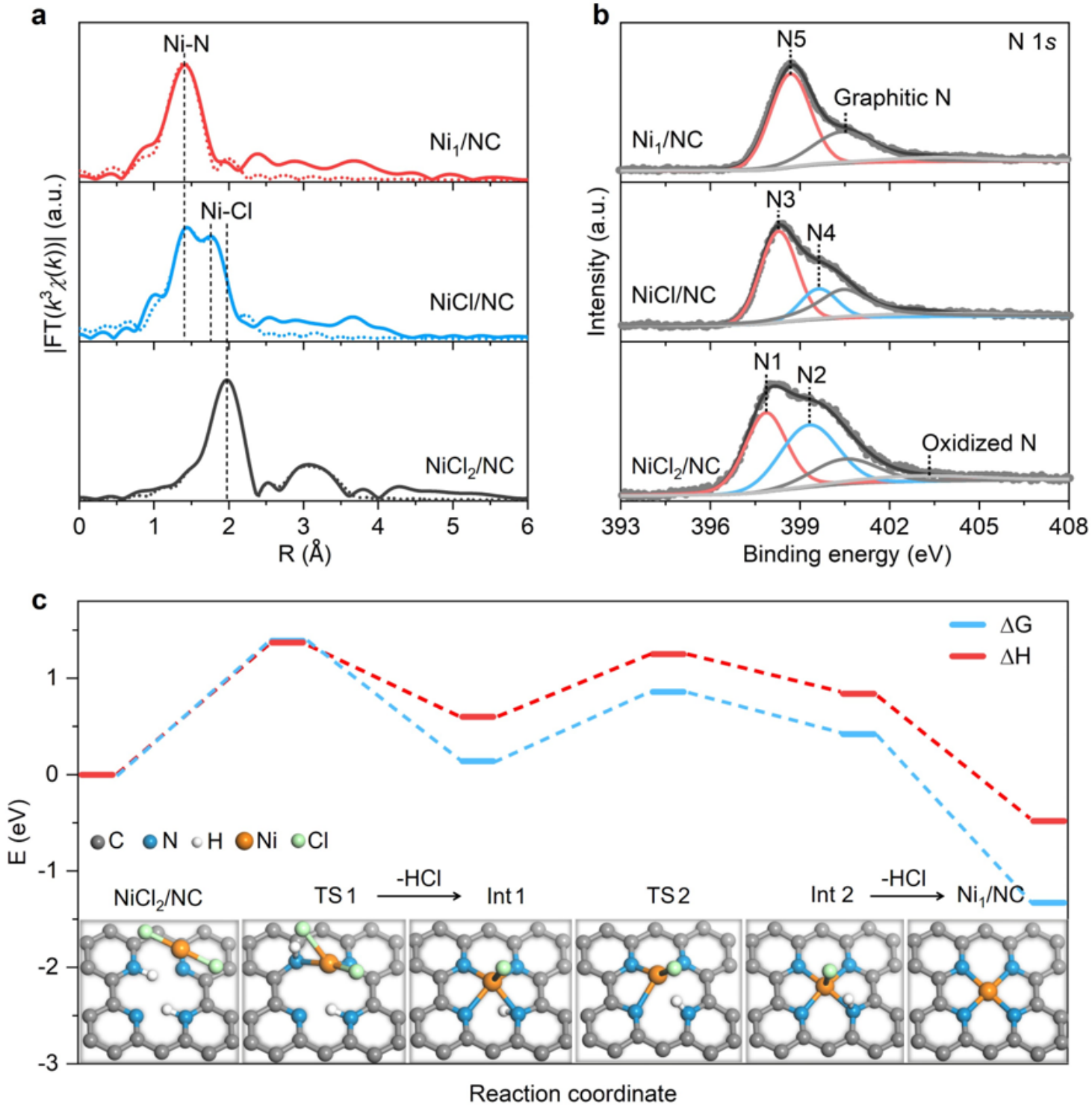

Figure 5

Mechanistic investigation of the synthesis of UHD-SACs. a, b, Fourier transformed EXAFS (a) and N 1s XPS (b) spectra of NiCl2/NC, NiCl/NC and Ni1/NC. c, DFT calculated energy pathway for the formation of Ni-N4 from the NiCl2 precursor with representative transition states and intermediates depicted inset.

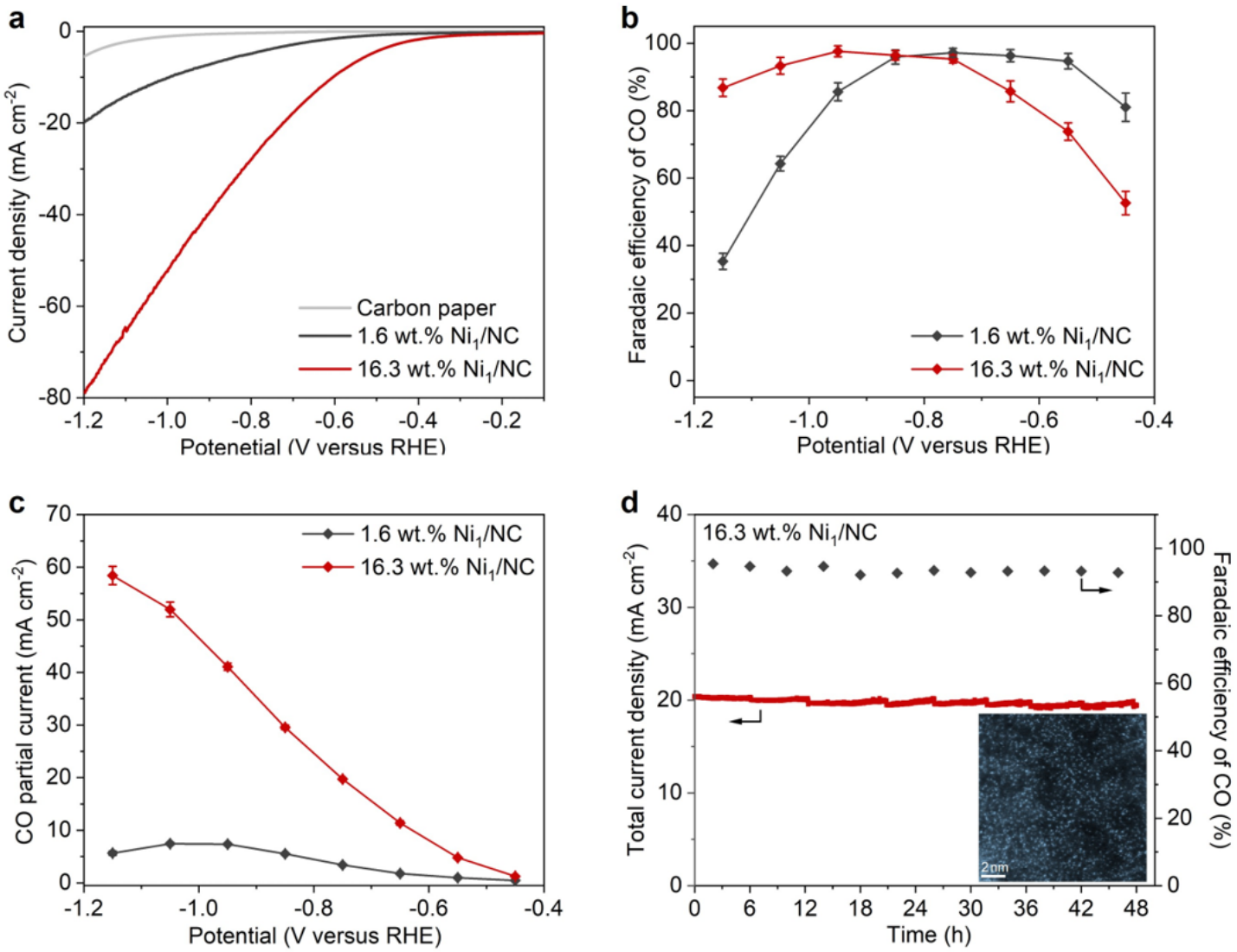

Figure 6

Electrocatalytic CO2 reduction reaction performance. a, Linear sweep voltammetry curve b, Faradic efficiency and c, CO partial current density over 1.6 wt.% and 16.3 wt.% Ni1/NC catalysts. d, Stability test of 16.3 wt.% Ni1/NC UHD-SAC. The inset shows an atomic-resolution ADF-STEM image of the catalyst after the reaction, confirming the preserved single-atom dispersion.

Supplementary Files

This is a list of supplementary files associated with this preprint. Click to download.

- Supplementaryinformation.docx